Role of Alloying Elements in Passive and Transpassive Behavior of Ni-Cr-Based Alloys in Borate Buffer Solution

Zhiheng Zhang, Benoît Ter-Ovanessian, Sabrina Marcelin, Jules Galipaud, Bernard Normand

Journal of The Electrochemical Society

Role of Alloying Elements in Passive and Transpassive Behavior of Ni–Cr-Based Alloys in Borate Buffer Solution

Journal of The Electrochemical Society, 2021 **168** 081503

Role of Alloying Elements in Passive and Transpassive Behavior of Ni–Cr-Based Alloys in Borate Buffer Solution

Zhiheng Zhang,[1] Benoît Ter-Ovanessian,[1,*,z] Sabrina Marcelin,[1] Jules Galipaud,[1,2] and Bernard Normand[1]

[1] *Université de Lyon, Institut National des Sciences Appliquées de Lyon, MATEIS UMR CNRS 5510, Villeurbanne cedex, France*
[2] *Université de Lyon, Ecole Centrale de Lyon, LTDS UMR 5513, Ecully, France*

The role of the alloy composition of binary Ni–xCr alloys (x = 16, 20, 24, 28 wt.%) and ternary Ni–xCr–8Fe alloys (x = 14, 22, 30 wt.%) in borate buffer solution on the passive and transpassive behavior was investigated using successive electrochemical impedance measurements. These measurements supplement conventional polarization curves by enabling monitoring of the evolution of the electrochemical parameters extracted from impedance diagrams (thickness, resistivity at interfaces, etc) during the polarization. The polarization curves and evolution of the impedance parameters revealed that the Cr content and addition of Fe did not significantly affect the behavior of the alloys within the passive potential domain but directly affected the transpassivation process at higher potentials. For the Ni–xCr alloys, a higher Cr content resulted in a higher current-density peak for the transpassivation–second passivation processes. Conversely, the addition of Fe reduced or even prevented the appearance of this current-density peak. X-ray photoelectron spectroscopy analysis provided complementary information to help explain the role of alloying elements in the passivation (and secondary oxidation) mechanisms of Ni-based alloys in borate buffer solution.
 [DOI: 10.1149/1945-7111/ac1890]

Manuscript submitted April 28, 2021; revised manuscript received June 22, 2021. Published August 5, 2021.

Supplementary material for this article is available online

Nickel-based alloys are widely used for critical applications because of their ability to form passive films in aqueous environments and protective oxides with controlled growth rates at high temperature. Moreover, they exhibit favorable and tunable mechanical properties. However, the design of novel nickel-based alloys remains a challenge given the complexity of the chemical and mechanical loadings potentially encountered in advanced applications, such as those in the nuclear and aerospace domains.

The corrosion resistance of these alloys can be greatly improved through the addition of certain alloying elements such as Cr, which acts as a passivity promoter, supporting the nucleation of the oxide.[1] The Cr-rich layer within the passive film is considered the main corrosion-resistance feature of these alloys.[2] The oxide films on Ni–Cr binary alloys have generally been reported to consist of a main Cr oxide network mixed with a minor Ni oxide network or the insertion of a certain concentration of metal ions.[3] Moreover, a dual structure is generally considered to be formed by an inner oxide part and an outer hydroxide part consisting of both metallic elements.[4] Cr (III) is the main cation species in both layers, whereas Cr(VI) and Ni (II) are the minor species.

The minimal concentration of Cr required for passivity in bulk Ni–Cr alloys has been determined to be 8–11 at.%.[5] In acidic solution, the passivation potential is shifted to more negative values with increasing Cr content. The current densities in the active and passive potential ranges decrease with increasing Cr content.[6] However, a critical Cr concentration of 22–26 wt.% in bulk Ni–Cr alloys enables the diffusivity of charge species within the passive film to be tailored, maintaining a low steady-state current density and ensuring good resistance to the passivity breakdown process.[7] In chloride-containing solution, a similar Cr concentration provides good resistance to pitting corrosion, limiting the nucleation and growth of pits.[8] However, the potential range of passivity is affected by the Cr content. Indeed, the transpassive potential is generally lower for Ni–Cr alloys than for pure Ni which exhibits a transpassive region for potential located after thermodynamic water stability.[4]

Transpassivation is characterized by a rapid dissolution of metal or alloy when the electrode potential becomes too positive.[9] The transpassive oxidation potential is thermodynamically controlled. It is mainly dependent on the aqueous solution (essentially the pH). For Ni–Cr-based alloys, this thermodynamic phenomenon is linked to the redox potential of Cr(III) to Cr(VI) generally expressed as.[4]

$$Cr_2O_3 + 10OH^- \rightarrow 2CrO_4^{2-} + 5H_2O + 6e^- \quad [1]$$

However, in basic solution, the transpassive dissolution rate can be limited by the formation of a new oxide film on the surface that contains chemical species in a higher valence state. This phenomenon is called secondary passivation.[10] Figure. 1, adapted from our previous study[11] presents the polarization curves obtained for a synthetic Ni–Cr binary alloy (with 20 wt.% Cr) immersed in 10 g l^{-1} Na_2SO_4 acidified with H_2SO_4 (pH = 2) (red curve) and in 0.05 M H_3BO_3 + 0.075 M $Na_2B_4O_7$ $10H_2O$ (pH = 9.2) (blue curve). In acidic solution, the alloy presents a higher corrosion potential and wide passive range and a transpassive process, whereas in borate buffer solution, the alloy exhibits a lower corrosion potential and a transpassivation–secondary passivation transition, as evidenced by the hump in current density after the passive domain. The secondary passivation is not always observed in polarization curves. Mishra et al.[12,13] showed that the occurrence and intensity of this phenomenon are closely related to the pH and oxyanion of the solution. They proved that the full process, including the apparent breakdown of the passive film followed by an anodic peak and a secondary passive region, occurs for Cr-containing Ni-based alloys for solutions with pH > 8.6, such as carbonate/bicarbonate or borate buffer solutions. They also reported that for Ni–Cr–Mo alloys, the apparent transpassive potential and anodic peak potential are independent of the chemical composition of the alloy. However, the current densities of the anodic peak and secondary passive plateau are affected by the solution and alloy chemistry.

In the present work, the relation between the passive and transpassive behaviors and the chemical composition of synthetic Ni-based alloys is addressed, focusing on the role of not only the Cr content but also the Fe content. Indeed, Fe is generally added as an alloying element in Ni-based alloys because it reduces the total cost

*Electrochemical Society Member.
[z]E-mail: benoit.ter-ovanessian@insa-lyon.fr

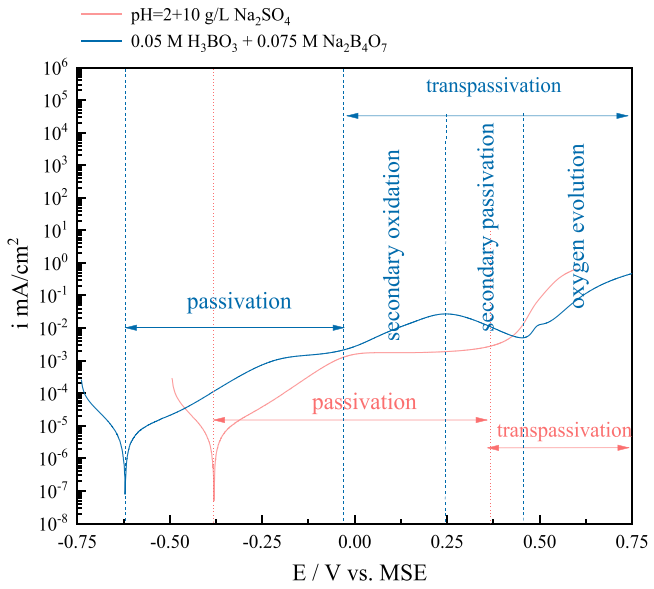

Figure 1. Potentiodynamic polarization curves obtained for Ni–20Cr binary alloy in aerated acidic and buffer solutions (scan rate of 0.5 mV s^{-1} after 24 h of immersion).

of the material while improving the machinability and weldability. Even if Fe contributes to the passive film formation, the addition is not straightforwardly beneficial to the corrosion behavior of Ni-based alloys. For example, in acidic solution, adding 8 wt.% Fe to Ni–Cr binary alloys increases the current density of the active peak and the passive plateau.[14] In acidic saline solution, the ternary Ni–Cr–Fe alloy was more sensitive to pitting corrosion than the binary Ni–Cr alloy even though the thickness of the passive film was not remarkably changed and only minor amounts of Fe were detected.[15] In basic solution, Boudin et al.[16] confirmed that the passive film thickness was unchanged by the addition of Fe and that the oxidized Fe mainly appeared in the mid-part of the passive film. Moreover, the addition of Fe to Ni-based alloys has been shown to decrease the corrosion currents in the transpassive potential range;[17] however, this finding is not yet well understood.

Considerable research has been conducted on the passivation of binary Ni–Cr and ternary Ni–Cr–Fe alloys;[2,6–8,17] however, the growth mechanism and the nature, composition, and structure of the passive films during polarization processes remain largely unexplored. Moreover, most prior investigations on the corrosion behavior of passive alloys have focused on the passive regime, with little attention paid to the transpassive phenomenon and the key parameters governing it. A relatively high potential is required to activate transpassive dissolution; nevertheless, certain service conditions (accidents, radiolysis,…) can shift the potential,[18] resulting in transpassive dissolution and consequently shortening the service life of alloys. Moreover, Chiang et al. suspected that the susceptibility to stress corrosion cracking may be related to the active dissolution due to transpassivation.[19] Hence, preventing damage from transpassive dissolution is of considerable interest in the corrosion domain.[20] A better understanding of the passivation process and mechanism when the applied potentials change, even in the transpassive and secondary passivation regimes, could provide insight into the key factors of success for the design of new alloys.

In such a context, the aims of the current work were to demonstrate the role of alloying elements in the electrochemical behavior of Ni–based model alloys by following the features of passivation and transpassivation with polarization over a wide potential range. Successive electrochemical impedance measurements were performed on various binary Ni–Cr and ternary Ni–Cr–Fe alloys in borate buffer solution. Thanks to recent advances in the analysis of electrochemical impedance spectra, successive electrochemical impedance measurements provide insight into the chemical processes occurring during passivation and polarization processes.[21] Using this approach, a better understanding of the effect of the alloy composition (Cr and Fe content) on the electrochemical behavior of Ni-based alloys from cathodic potential to the transpassive region was attained. In addition, the roles of the alloying elements in the secondary passivation process and especially in determining the chemical composition of the passive film were studied in detail using X-ray photoelectron spectroscopy (XPS).

Experimental

Material and surface preparation.—To investigate the effect of Cr content on the passivation behavior of Ni-based alloys, Ni–xCr (x = 16, 20, 24, 30 wt%) model alloys were selected. Moreover, Ni–xCr–8Fe (x = 14, 22, 30 wt%) model alloys were also studied to determine the contribution of Fe in passivation processes. These materials were supplied by Sumitomo Metal Industries, Ltd. Japan. All the model alloys had an austenitic structure without the presence of carbides. Pure chromium (> 99.7 wt.%), supplied by Goodfellow served as a reference material. The chemical compositions (wt.%) of the alloys are presented in Table I.

The samples were ground with abrasive papers up to 4000 grit with mirror polishing down to 1 μm for the electrochemical tests, cleaned with deionized water and ethanol, respectively, and finally dried with flowing argon.

Electrochemical measurements.—Electrochemical measurements were performed on a Gamry Reference 600 electrochemical potentiostat. A conventional three-electrode cell was used for the electrochemical measurements. The different model alloys were used as the working electrode (exposure area = 0.56 cm^2). A large graphite rod served as the counter electrode, and a saturated mercury sulfate electrode (MSE, E = +658 mV vs SHE) acted as the reference electrode. A naturally aerated solution of 0.05 M H_3BO_3 + 0.075 M $Na_2B_4O_7$ $10H_2O$ (pH = 9.2) was prepared for the electrochemical tests. This solution has been widely used to investigate the passive behavior of Ni–Cr alloys and stainless steel because Cr-rich oxides and hydroxides have a low solubility in the borate solution.[22–24] All the electrochemical measurements were performed at 22 ± 3 °C in a temperature-controlled testing room.

First, the open-circuit potential (OCP) was monitored for 24 h to achieve stability of the interface of the passive film/borate buffer

Table I. Chemical compositions (wt.%) of binary and ternary model alloys.

Alloys	C	Mg	Si	P	S	Cr	Mn	Fe	Ni
Ni–16Cr	0.006	0.008	<0.001	0.002	<0.001	15.7	0.049	0.015	Bal.
Ni–20Cr	0.008	0.005	0.009	0.001	<0.001	19.8	0.045	0.018	Bal.
Ni–24Cr	0.004	0.003	0.008	0.001	<0.001	23.8	0.047	0.027	Bal.
Ni–28Cr	0.006	0.001	0.006	0.001	<0.001	27.6	0.045	0.024	Bal.
Ni–14Cr–8Fe	<0.001	0.001	0.02	0.001	<0.001	14.7	0.05	7.81	Bal.
Ni–22Cr–8Fe	<0.001	0.001	0.02	0.001	0.001	21.6	0.05	7.84	Bal.
Ni–30Cr–8Fe	<0.001	0.002	0.02	0.001	0.001	29.4	0.05	7.85	Bal.

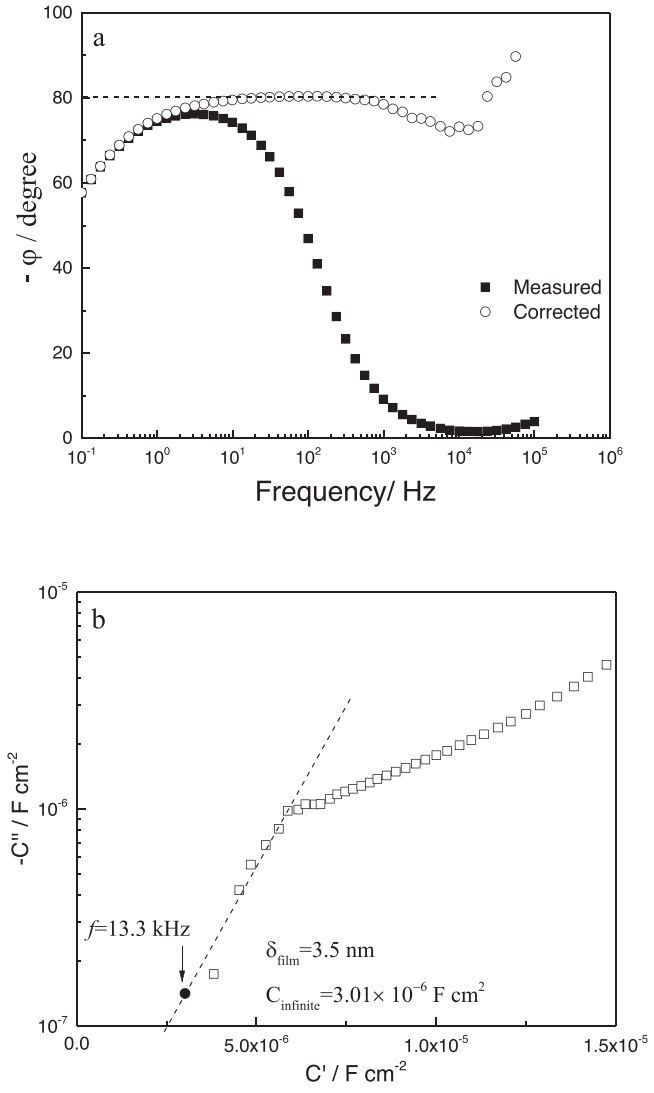

Figure 2. (a) Electrolyte resistance corrected Bode diagram obtained at −0.1 V vs MSE for Ni16Cr, and (b) Estimation of thickness of passive film formed using infinite capacitance (C_∞) from the complex representation for similar alloy and experimental conditions.

solution. Then, successive electrochemical impedance measurements were performed. Increases in the potential in step sizes of 50 mV in the anodic direction were sequentially applied, starting from −0.1 V vs E_{OCP} and ending at +1.2 V vs E_{OCP}. Each potential was maintained for 120 s to achieve pseudo-stationarity and was followed by an electrochemical impedance measurement in a narrower frequency range (10 kHz to 0.1 Hz), with 8 points per decade and a sine wave with 10 mV amplitude. These optimal measuring parameters were selected on the basis of a previous investigation[11]

Surface analysis.—XPS analysis was performed to characterize the chemical compositions of the passive films using an ULVAC-PHI Versaprobe II spectrometer with a monochromatic Al Kα (1486.6 eV) source. The take-off angle was kept constant at 45° during the measurement. Dual-beam neutralization was employed for charge compensation. The aliphatic carbon peak at 284.8 eV of adventitious carbon in the C1s region was used to adjust the remaining charge. A pass energy of 23 eV was used for the high-resolution spectra. Fitting and quantification were performed using CasaXPS software with the relative sensitivity factors extracted from Ref.[25]. The studied passive films were formed on the Ni–16Cr and Ni–14Cr–8Fe alloys at potentials of −0.1 ± 0.02 V, 0.1 ± 0.02 V, and 0.4 ± 0.02 V vs MSE, corresponding to the stable passivation, secondary oxidation, and secondary passivation regions, respectively. These two alloy compositions were selected to verify and illustrate the change of composition of the passive film with the addition of Fe in the different potential regions. The samples were polarized for 12 h at each selected potential to reach steady state of the passive films.

Theoretical Approach

The electrochemical impedance diagrams were analyzed as a function of the potential domain using two complementary approaches. Enhanced graphical determination of the impedance parameters was performed for the entire potential range studied, whereas the impedance diagrams were fitted using the power law model (PLM) only within the potential range of the passive domain. The equivalent electrical circuit applied and the related assumptions were discussed in our previous study.[11,26,27]

Graphical determination.—As generally noted for impedance data on passive materials, a distorted capacitive behavior was observed over a wide range of high frequencies, suggesting a constant phase element (CPE) behavior. The CPE parameters (α and Q_{eff}) were obtained using the enhanced graphical method.[28] The effective CPE exponent α was estimated from a modified phase angle–frequency Bode representation after determination of the electrolyte resistance ($R_{e,est}$)

$$\varphi_{adj} = \tan^{-1}\left(\frac{Z''}{Z' - R_{e,est}}\right) \quad [2]$$

where φ_{adj} is the phase angle corrected by the electrolyte resistance, and Z' and Z'' are the real and imaginary parts of the impedance, respectively. For $\alpha < 1$, the CPE parameter α can be determined using the following equation

$$\varphi_{adj} = -90°\alpha \quad [3]$$

An example of electrolyte corrected Bode diagram is presented in Fig. 2a. The effective CPE coefficient (Q_{eff}) can be determined from the imaginary part of the impedance in the considered frequency range, with the angular frequency $\omega = 2\pi f$[29]

$$Q(\omega) = \sin\left(\frac{\alpha\pi}{2}\right)\frac{-1}{Z''\omega^{\alpha}} \quad [4]$$

Thus, the complex-capacitance representation emphasizes values at high frequency, enabling determination of the high-frequency limit of the real part of the complex capacitance. The complex capacitance adjusted by the electrolyte resistance representation can be expressed as[29]

$$C^* = \frac{1}{j\omega(Z - Z_{e,est})} \quad [5]$$

The high-frequency-limit capacitance is related to the dielectric field within the passive film.[30] An example of complex capacitance diagram after adjustment by the electrolyte resistance is shown in Fig. 2b. Hence, the thickness of the passive film (δ) can be estimated from the high-frequency-limit capacitance (C_∞)[31]

$$\delta = \frac{\varepsilon\varepsilon_0}{C_\infty} \quad [6]$$

where ε is the dielectric constant of the oxide ($\varepsilon = 12$ for Cr_2O_3)[32] and ε_0 is the vacuum permittivity (8.85×10^{-14} F cm^{-1}). The excellent agreement between the estimated thickness determined with this method and the ones calculated from XPS measurement has already been proved.[11,31]

Table II. Obtained parameters from impedance diagram analysis.

Obtaining way	Parameters
From graphical determination	α[a)], Q_{eff}[a)]
From calculation	Thickness[a)], (Resistivity ρ_δ[b)])
From fitting procedure	Resistivity ρ_0[b)]
	Resistivity ρ_δ[b)]

a) for all impedance diagrams. b) Only in passive domain.

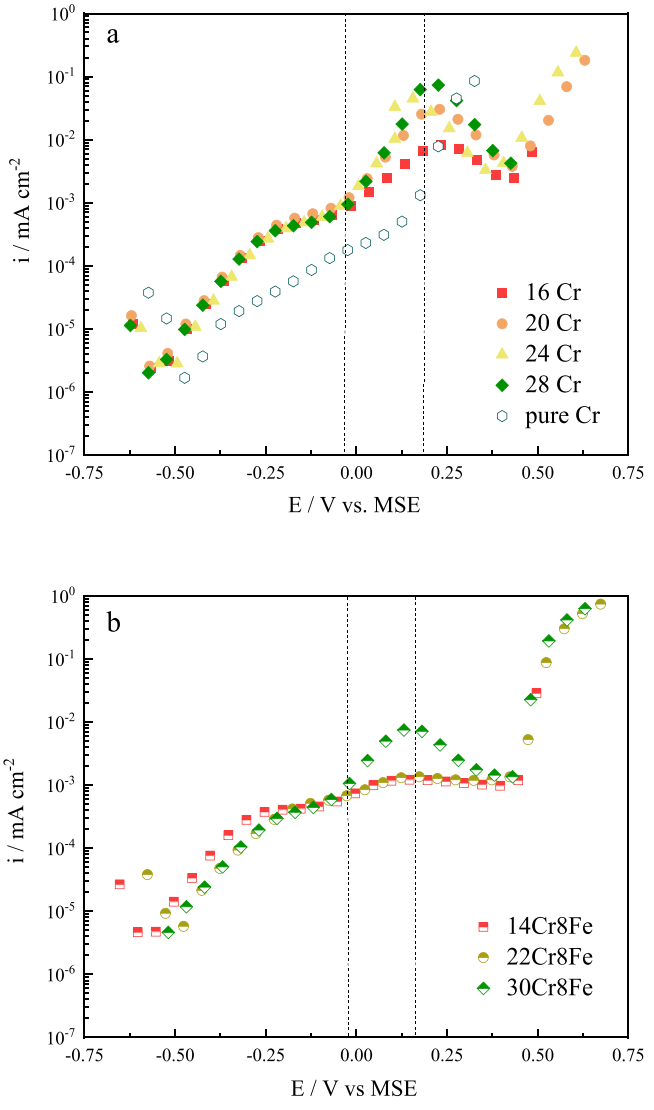

Figure 3. Potentiostatic polarization curve for (a) binary Ni–xCr alloys (x = 16, 20, 24, 28 wt%) and pure Cr, (b) ternary Ni–xCr–8Fe alloys (x = 14, 22, 30 wt%), obtained in aerated 0.05 M H_3BO_3 + 0.075 M $Na_2B_4O_7$ $10H_2O$ borate buffer solution at pH = 9.2.

Power law model for passive film.—In the PLM, the CPE behavior is attributed to the variation of the resistivity with the passive film thickness according to a power law;[33,34] thus, it is a good candidate for describing the passive film. Under the assumption that the permittivity through the passive film is constant, the resistivity profile is given by

$$\frac{\rho}{\rho_\delta} = \left(\frac{\rho_\delta}{\rho_0} + \left(1 - \frac{\rho_\delta}{\rho_0}\right)\xi^\gamma\right)^{-1} \quad [7]$$

where ρ_δ is the resistivity at the passive film/electrolyte interface; ρ_0 is the resistivity at the alloy/passive film interface; and ξ is the dimensionless position $\xi = x/\delta$, where x corresponds to the depth position of the passive film. γ is calculated from the CPE parameter α ($\gamma = 1/(1-\alpha)$) and indicates how sharply the resistivity varies. The integrated expression of the film impedance can be written as follows[33]

$$Z(\omega) = g\frac{\delta\rho_\delta^{1-\alpha}}{(\rho_0^{-1} + j\omega\varepsilon\varepsilon_0)^\alpha} \quad [8]$$

where

$$g(\alpha) = 1 + 2.88\left(\frac{1}{1-\alpha}\right)^{-2.375} \quad [9]$$

When the cathodic contribution is non-negligible, a charge-transfer resistance is set in parallel to the PLM impedance to adjust the impedance data.

Impedance diagram analyzing strategy.—The non-commercial software SIMAD (LISE UMR 8235 CNRS, Sorbonne University, Paris) was used to fit the impedance data. The graphical determination and the regression process are complementary as the enhanced graphical representation is valuable for determining at least three parameters needed for fitting with the PLM. Indeed, for all the impedance diagram obtained in this study, the CPE parameters (α and Q_{eff}) were obtained by graphical determination while the thickness was calculated from complex capacitance extrapolation. Then, for the regression with SIMAD, the graphically determined or calculated values were used as input data and fixed parameters. Only resistivities (ρ_δ) and (ρ_0) were then regressed. Finally, all the parameters were regressed by a simplex method around the initial values to minimize the fitting errors. Using this analyzing procedure insure the reliability between the graphically determined parameters and the regressed ones. Table II reports the different parameters and their obtaining way from impedance diagram analysis.

Results and Discussion

The results obtained from the successive electrochemical impedance measurements were intentionally separated into the study of the polarization curves and the investigation of the evolution of the electrochemical parameters determined through analysis of the impedance spectra.

Current density–potential curves.—Figure 3a presents the polarization curves for the Ni–xCr alloys (x = 16, 20, 24, 28) and pure Cr in aerated borate buffer solution obtained by step-by-step potentiostatic measurements. The reported current density is the average value of the last ten measurements for each potential step. For all the curves, the corrosion potential was close to −0.6 V vs MSE. The shapes of the polarization curves of the Ni–xCr alloys with different Cr contents were similar, especially in the passive domain defined between −0.6 V and 0 V vs MSE. For more anodic overvoltage, a hump in the current density related to the second oxidation and repassivation followed by a final increase of the current density was observed. Anodic current densities of the same order of magnitude were observed in the passive range regardless of the Cr content in the binary alloy. This result suggests that the passive behavior characterized in the borate buffer solution remains almost independent of the Cr content. However, the critical current density measured at 0.23 V vs MSE for the Ni–16Cr, Ni–20Cr, Ni–24Cr, and Ni–28Cr alloys was 0.008, 0.03, 0.04, and 0.07 mA cm^{-2},

respectively. Notably, for all the tested materials, the current-density peak increased with increasing Cr content; however, the current density corresponding to the second passivation plateau remained the same. For comparison, the polarization curve for pure Cr was obtained under the same conditions. Notably, no secondary passivation phenomenon was observed in this case. Only transpassive dissolution, indicated by the continuous increase of the current density for potentials higher than 0.20 V vs MSE, was observed. Consequently, the second oxidation–repassivation transition was induced by the Ni matrix that plays a role in this potential domain, allowing the repassivation phenomenon.[35] It is worth mentioning that in this potential range, Ni remains in a passive state.[36,37]

Similar polarization curves were obtained for the ternary Ni–xCr–8Fe alloys (x = 14, 22, 30 wt%), as presented in Fig. 3b. The corrosion potentials for all the alloys were close to the value of −0.6 V vs MSE of the binary alloys. Moreover, the current-density plateau for the ternary alloys had the same order of magnitude. With the addition of Fe, the corrosion tendency in the passive region was not changed. These findings suggest that the passive film grown in borate buffer solution behaved similarly for all the materials tested within the passive domain and that the barrier property of the passive film should be attributed to a similar inner layer. However, interestingly, the dissolution–repassivation peak for the Ni–14Cr–8Fe and Ni–22Cr–8Fe alloys was almost absent in the secondary passivation domain compared with that of the Ni–Cr binary alloys. For these two materials, a smooth evolution of the current density was observed at 0.0 V vs MSE before a plateau of 1 μA cm^{-2} was reached, indicating a slight evolution of the interface. In contrast, the dissolution–repassivation peak still existed for the Ni–30Cr–8Fe alloy, and the critical current density near 0.13 V vs MSE was 7 μA cm^{-2}. Thus, the addition of Fe has a beneficial role in the electrochemical behavior, limiting the current density in the transpassive potential domain, consistent with findings in the literature.[17] This effect is also suggested for the corrosion behavior of stainless steel.[38,39]

XPS characterization.—To determine the representative effect of Fe addition on the passive and transpassive behavior, XPS was used to analyze the compositions of the passive films grown at three different potentials on binary Ni–16Cr and ternary Ni–14Cr–8Fe alloys. Indeed, the current density measured on Ni–16Cr revealed the presence of a secondary oxidation peak and secondary passivation, which were not observed for the Ni–14Cr–8Fe alloy (Fig. 3). The applied potentials were −0.1 V, 0.1 V, and 0.4 V vs MSE, corresponding to the domains of passivation, transpassivation, and secondary passivation, respectively. The high-resolution spectra of Cr 2p3/2, Ni 2p3/2, O 1s, and Fe 2p3/2 regions of the passive films were analyzed. The fitted spectra and binding energies corresponding to the different chemical elements are presented in the Appendix supplementary data(available online at stacks.iop.org/JES/168/081503/mmedia). The main components of the passive films formed at different potentials on two samples are summarized in Fig. 4. Only information on the oxides and hydroxides was included, and that on the metallic components was excluded. In addition, Table III reports the ratio of oxides to hydroxides for the different components in the passive films formed at different potentials.

In Fig. 4a, at the applied potential of −0.1 V vs OCP, Cr_2O_3 and $Cr(OH)_3$ were detected for Cr and NiO and $Ni(OH)_2$ were detected for Ni. For the three potentials, the passive films consisted of a mixed oxide–hydroxide layer. The total oxide/hydroxide ratio was close to 1.27 for −0.1 V vs MSE, decreased to 0.52 at 0.1 V vs MSE, and increased to 1 at 0.4 V vs MSE, indicating that more hydroxide formed in the transpassivation process. For the last two potentials, the Cr_2O_3 signal was lower than that at −0.1 V vs MSE. The Ni hydroxide enrichment was only observed at 0.1 V vs MSE, corresponding to the dissolution potential. A similar result has been reported in the literature.[12,13] At this potential, the oxide CrO_3 was detected, confirming that Cr^{6+} is generated during polarization at this potential and partially remains within the film. At the potential of 0.4 V vs MSE, the signal of the metallic state became more pronounced (see Appendix a.3), indicating that the layer was thin.[40] The passive film was thinner at high anodic potential, and there was less Cr in the film.

XPS analysis of the ternary Ni–14Cr–8Fe alloy, shown in Fig. 4b, revealed that the chemical composition of the passive layer was more complex. The main oxide–hydroxide networks remained enriched in Cr, Ni, and Fe, contributing to the passive layer in both oxide and hydroxide forms and at different oxidation states. The contents of chromium oxide Cr_2O_3 and hydroxide $Cr(OH)_3$ in the passive film at 0.4 V vs MSE were lower than those at the other two potentials. It is worth mentioning that CrO_3 was not detected in the passive film formed at the three potentials. Moreover, Ni hydroxide was the main component at 0.4 V vs MSE. The overall contribution of Fe increased from −0.1 V vs MSE to 0.1 V vs MSE. Additionally, Fe_2O_3 was not detected at 0.4 V vs MSE, and a higher FeOOH content was observed. These results indicate that the combination of Ni and Fe plays a significant role in the passive film behavior at high anodic potentials by modifying the oxide layer and limiting the dissolution of the material, especially forming hydroxides at 0.4 V vs MSE, thus preserving the passivity.

Evolution of EIS parameters determined graphically during anodic polarization.—The evolution of the graphically determined CPE exponent α with potential for the Ni–xCr alloys (x = 16, 20, 24, 28 wt%) and pure Cr is shown in Fig. 5a1. Regardless of the chromium content, the α values were similar with the same evolution trend with the applied anodic potential. The CPE parameter remained stable at approximately 0.92 in the potential range between −0.6 V and −0.25 V vs MSE, followed by a decrease to 0.85 at 0.05 V vs MSE. In the potential range defined by the secondary oxidation for Ni–Cr alloys, α increased continuously, reaching approximately a plateau at 0.89 at 0.3 V vs MSE for 16Cr and 0.83 for 28Cr. Finally, for more anodic potential, α decreased again. This evolution provides relevant indications about the reactivity of the Ni–xCr alloys. First, in the passive domain, the passive film was modified when the potential increased, even before the occurrence of the transpassive dissolution, suggesting a continuous alteration of the passive film to breakdown. Then, during the second oxidation, transpassive dissolution occurred and was followed by a novel oxide formation, limiting the current density. The CPE parameter α is linked with the dispersion of time constants related to surface heterogeneity or chemical composition distribution within the passive film. Consequently, both contributions of the passive film structure and electrochemical reactions modify the dispersion of time constants during polarization, resulting in the change of α value. In the potential domain related to second oxidation, α is dependent of the Cr content in the Ni–xCr alloys, suggesting that the structure or chemical composition of the oxide layer is different from that of the original passive film or that the transpassive dissolution kinetics is affected by the Cr content. For comparison, α for the pure Cr remained over 0.9 in this passive potential range but decreased all the time within the transpassive region. No increase of α was observed because no secondary passivation was detected during the measurement. The evolution of the second CPE parameter Q_{eff} with potential for the Ni–xCr alloys and pure Cr presented in Fig. 5b1 is consistent with a continuous evolution of the passive layer up to −0.05 V vs MSE, followed by a slightly different evolution within the second-oxidation domain. For pure Cr, this second trend was less observable, as no second passivation occurred. The final increase of Q_{eff} is related to the complementary contribution of the double-layer capacitance associated with the reaction of water oxidation. It assumes that CPE probably consider the capacitance of the passive layer and double layer capacitance contributions when the water oxidation reaction occurs. In this potential domain, the fitting model used previously is no longer valid and another time constant has to be introduced to consider the water oxidation reaction.

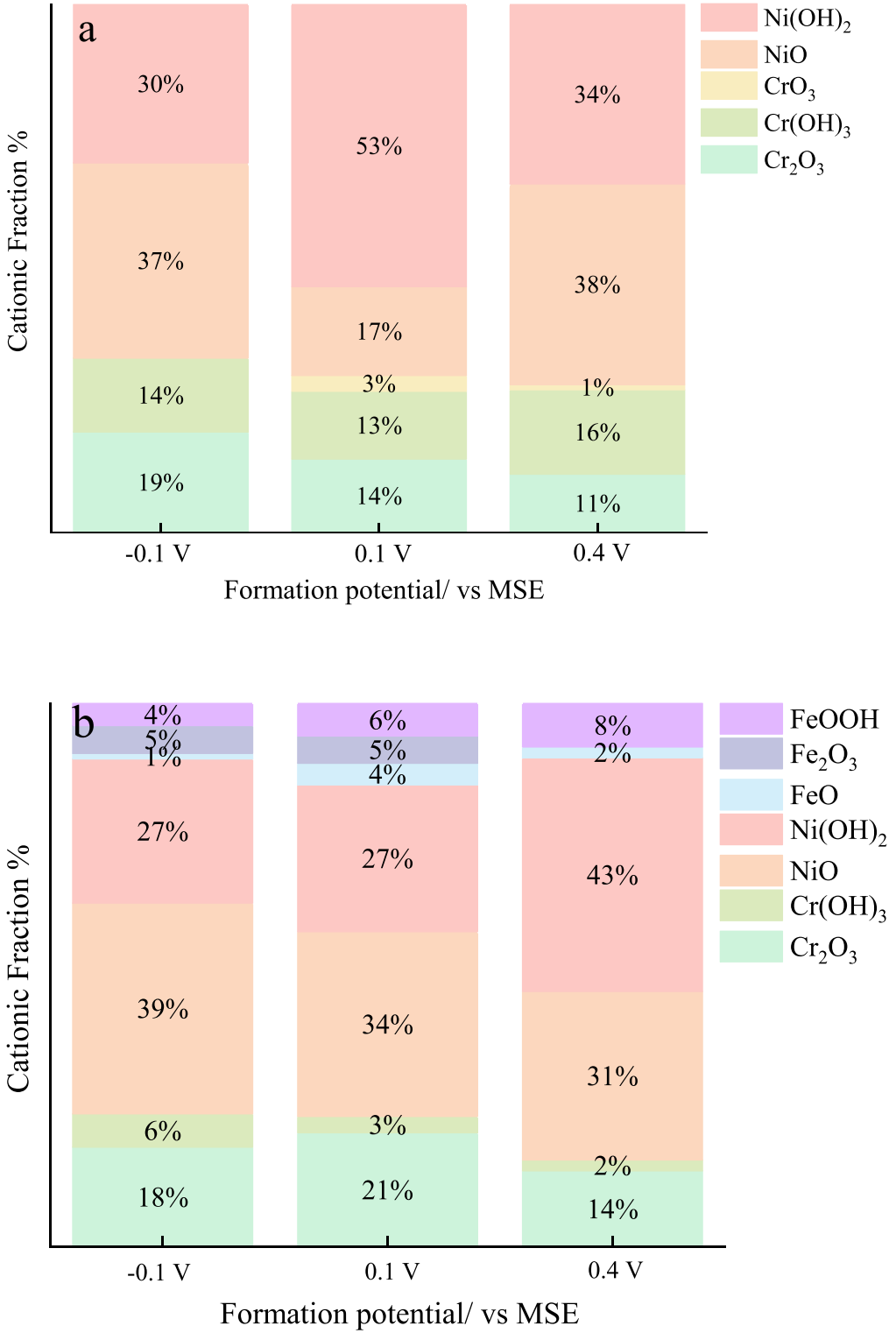

Figure 4. Main components of passive films formed on (a) Ni–16Cr alloy and (b) Ni–14Cr–8Fe alloys under different potentials in aerated 0.05 M H_3BO_3 + 0.075 M $Na_2B_4O_7$ $10H_2O$ borate buffer solution (pH = 9.2).

When Fe was added to the binary Ni–Cr alloy to obtain the Ni–xCr–8Fe alloys (x = 14, 22, and 30 wt%), the CPE parameter α showed a similar trend regardless of the tested material (Fig. 5a2). The value of α remained stable at approximately 0.92 in the potential range of −0.6 V to −0.25 V vs MSE, followed by a decrease to 0.85 at −0.05 V vs MSE. In the potential range of secondary oxidation, the value of α increased again, reaching approximately 0.89 at 0.3 V vs MSE. When the potential was nobler than 0.3 V vs MSE, α decreased again. Similar to the observation for the binary Ni–Cr alloys, the value of Q_{eff} for the Ni–xCr–8Fe alloys increased with applied potential (Fig. 5b2). These results indicate that the evolution trends of α and Q_{eff} are quite similar for binary and ternary alloys, whereas the polarization curves differ, especially in the domain of the second oxidation potential. However, the values of α in this potential domain were always higher for Ni–14Cr–8Fe and Ni–22Cr–8Fe than for the 30%wt Cr-containing alloy,

Table III. Ratio of oxide to hydroxide for the different metallic elements in passive films formed at different potentials.

$M_xO_y/M_{x'}(OH)_{y'}$	−0.1 V vs MSE	0.1 V vs MSE	0.4 V vs MSE
For Cr in Ni–16Cr	1.36	1.31	0.75
For Ni in Ni–16Cr	0.81	0.32	1.12
Total oxide/hydroxide in Ni–16Cr	1.27	0.52	1
For Cr in Ni–14Cr–8Fe	3.0	7.0	7.0
For Ni in Ni–14Cr–8Fe	1.44	1.26	0.72
For Fe in Ni–14Cr–8Fe	1.5	1.5	0.25
Total oxide/hydroxide in Ni–14Cr68Fe	1.7	1.78	1.13

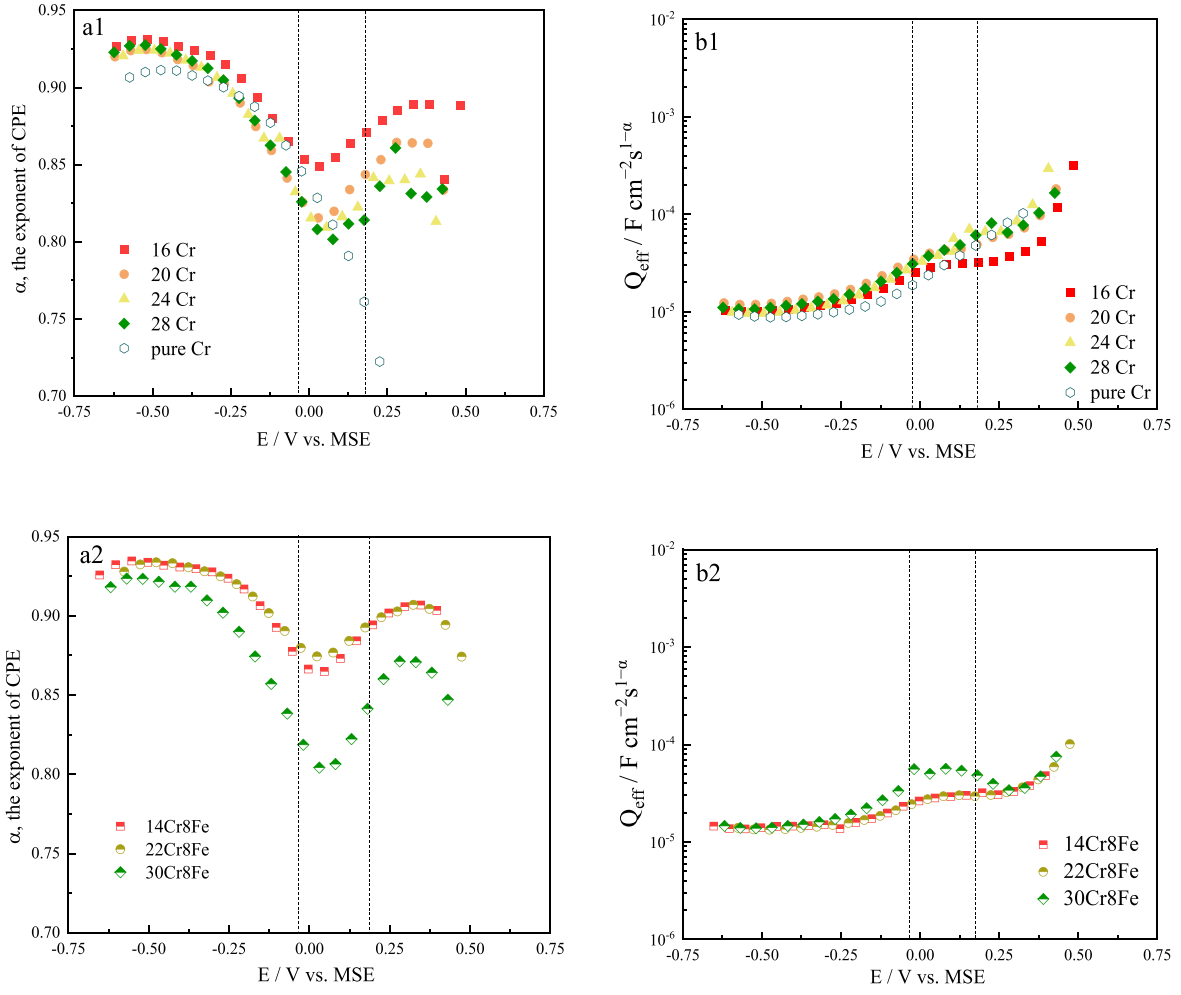

Figure 5. Evolution of CPE parameters α and Q_{eff} with potential for (a) binary Ni–xCr alloys (x = 16, 20, 24, 28 wt%) and pure Cr, (b) ternary Ni–xCr–8Fe alloys (x = 14, 22, 30 wt%) in 0.05 M H_3BO_3 + 0.075 M $Na_2B_4O_7$ $10H_2O$ borate buffer solution (pH = 9.2). Dotted lines represent the beginning of the transpassive phenomenon and the potential of the current density peak, respectively.

exhibiting a current-density peak. This finding suggests that Fe plays a role in the structure and chemistry of the oxide film within this potential range. When the Cr content was less than 30 wt.%, the dissolution of the passive film or the second oxidation kinetics of Cr was limited by the presence of Fe. Moreover, the higher value of α indicates that Fe contributes to a more homogenous oxide layer in the high potential region.

The evolution of the evaluated passive film thicknesses with potential for the Ni–xCr alloys (x = 16, 20, 24, 28 wt%) and pure Cr is shown in Fig. 6a. The deviation for the calculated thickness was approximately 9%. The deviation was calculated from the different estimations from the graphical determination for infinite capacitance. The evolutions of the passive film thicknesses for the four binary alloys show the same trend and can be separated into two parts. For the potentials below 0.0 V_{MSE}, there was no obvious change in thickness (a slight decrease). During polarization, the continuous increase of potential resulted in slight thinning of the passive films within the passive domain. The decrease of the thickness with applied anodic potential might be linked with the properties of the Cr oxide semiconductor grown on the Ni–Cr alloys.[21] Because the Cr oxide generally acts as a p-type semiconductor, the generation of cation vacancies was promoted during the polarization process. In the more anodic potential range (over 0.0 V_{MSE}), the thickness decreased rapidly, which could be linked to the transpassive reaction. The thicknesses were in the range of 3–4 nm for potentials between the cathodic domain and 0 V vs MSE, whereas that value for pure Cr was up to 6 nm. This result might have been caused by the presence of a larger amount of hydroxide in the passive film

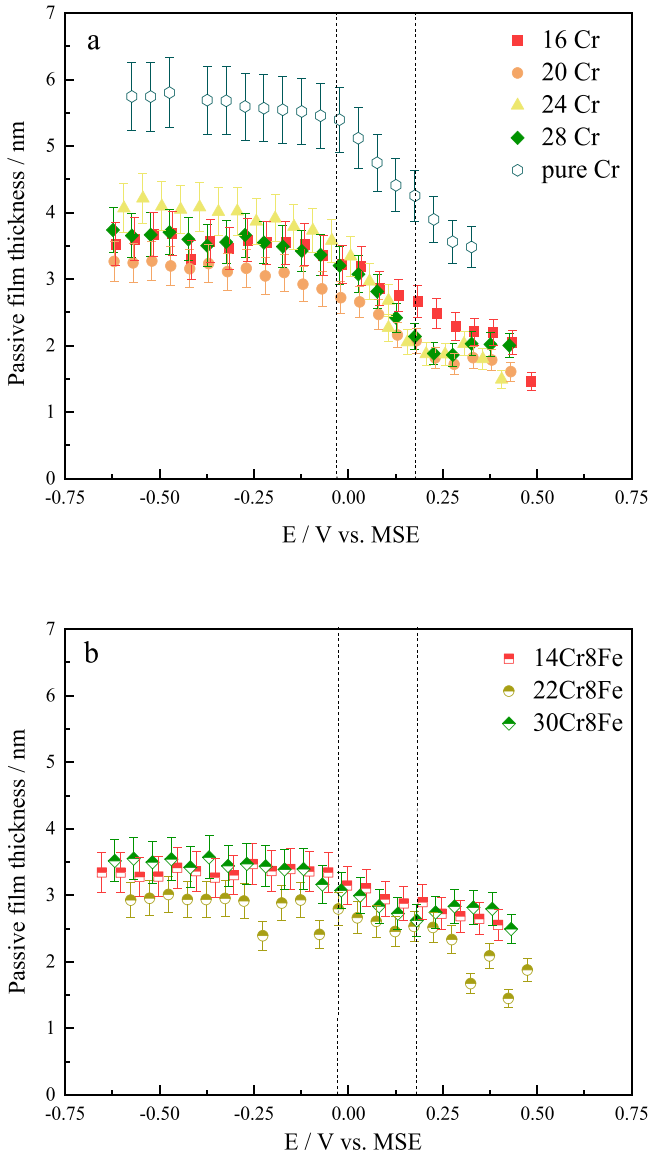

Figure 6. Evolution of calculated passive film thickness as a function of the applied potential for (a) Ni–xCr alloys (x = 16, 20, 24, 28 wt%) and pure Cr and (b) Ni–xCr–8Fe alloys (x = 14, 22, 30 wt%) in 0.05 M H_3BO_3 + 0.075 M $Na_2B_4O_7$ $10H_2O$ borate buffer solution (pH = 9.2). Dotted lines represent the beginning of the transpassive phenomenon and the potential of the current density peak, respectively.

formed on pure Cr in basic solution[41] he calculated thickness of the passive film for Ni–xCr alloys decreased to 1–1.5 nm at a potential of 0.5 V vs MSE.

Figure 6b shows the evolution of thickness of the passive films with the applied potential for the three ternary alloys. Interestingly, the passive films formed on the different Ni–xCr–Fe alloys were of similar thickness, which was close to that measured on the binary alloys. A similar result was also reported in the literature[42] and indicates that Fe is not the major element contributing to the passive layer. The calculated thickness of the passive films decreased from 3–3.5 nm at a potential near −0.6 V vs MSE to approximately 2 nm at the potential of 0.5 V vs MSE. The evolution of the passive layer thickness for the ternary alloys showed the same tendency as that of the binary alloys. The Fe oxide in the passive film is generally considered an n-type semiconductor.[43,44] As the evolution of the thickness trend was not changed by adding Fe, it can be considered that 8 wt.% Fe addition is not significant enough to change the semiconductor properties of the oxide on the Ni–xCr–Fe alloys. That is, the Fe oxide is incorporated in the Cr oxide network, which remains the main structure.

Resistivity profiles during anodic polarization.—The resistivities at the alloy/passive film interface (ρ_0) and passive film/electrolyte interface (ρ_δ) were obtained by adjusting the impedance diagram using the PLM. The evolution of these parameters could be studied similar to the previously presented parameters or by using a plot of the resistivity distributions within the passive film as a function of the potential. For the sake of clarity, monitoring of the evolution of the resistivity profiles of the Ni–16Cr and Ni–28Cr alloys was selected to study the effect of Cr content on the passivation behavior of Ni–xCr alloys. In addition, the resistivity profiles of Ni–14Cr–8Fe are presented for comparison with those of Ni–16Cr to study the role of Fe in the passivation behavior. For the same reason, certain potentials were selected to highlight the trend. However, it is important to note that regardless of the Cr content, both limit resistivities, ρ_0 and ρ_δ, follow the same tendency and the addition of Fe does not modify the trend of the evolution in the passive range.

Figure 7 shows the evolution of the resistivity distribution through the passive film for a selection of applied potentials for Ni–16Cr (Fig. 7a), Ni–28Cr (Fig. 7b), and Ni–14Cr–8Fe (Fig. 7c). For the three presented cases, the resistivity distribution profiles consist of two segments. The first segment is a plateau, where the resistivity is equal to ρ_0, starting from the alloy/passive film interface. The second segment corresponds to power-law decay of the resistivity, reaching the passive film/solution interface resistivity ρ_δ. This dual evolution of the resistivity can be linked with the dual structure of the passive film with an inner dense oxide layer and an outer hydrous layer. The length of the resistivity plateau can be considered the thickness of the inner dense chromium oxide, whereas the decay can be considered the electrolytic modified oxide–hydroxide.

The resistivity distributions for Ni–16Cr (Fig. 7a) and Ni–28Cr (Fig. 7b) present similar evolution trends. Both binary alloys have similar plateau lengths (up to 0.20), indicating that the interfaces between the passive film and alloys are similar and that the thickness of the inner layer is not affected by the Cr content. With increasing potential up to −0.07 V vs MSE, the length of the plateau decreases. There is a thinning effect of the inner layer even in the passive potential range. Concomitantly, ρ_0 also evolves. It decreases when the potential increases up to −0.22 V vs MSE. Then, between potentials of −0.22 V and −0.07 V vs MSE (corresponding to the plateau in the polarization curve in Fig. 3a), the limit resistivity ρ_0 remains stable. Finally, it decreases again close to the transpassivation potential. This evolution of ρ_0 suggests that this parameter is closely related to the anodic electrochemical reaction. Conversely, for both binary alloys, the resistivity ρ_δ at the passive film/solution interface shows an increasing tendency with applied anodic potential. The evolution of the resistivity ρ_δ indicates a continuous modification of the outer layer with the applied potential, suggesting the likely variation of the oxide/hydroxide ratio or the densification of this outer layer. This behavior might be caused by the consumption of more defects, which are present at the interface between the passive film and electrolyte. Moreover, it is also worth noting that the shape of the resistivity decay is smoother within the stable passivation domain, suggesting that the passive film is modified in depth during the anodic polarization and that the transition of the inner–outer layer is smoother. These evolution trends did not change with increasing Cr content.

In the resistivity profile of the ternary Ni–14Cr–8Fe alloy (Fig. 7c), the length of the plateau (up to 0.15) was shortened compared with that of the Ni–16Cr alloy (Fig. 7a). Similarly, as for the Ni–16Cr alloy, the length of the plateau decreased with increasing applied anodic potential and decreasing resistivity ρ_0 until the potential of 0.0 V vs MSE. In addition, ρ_δ at the interface between the passive film and electrolyte for the Ni–14Cr–8Fe alloy at the initial potential was 10^2 Ω cm, which is much lower than that

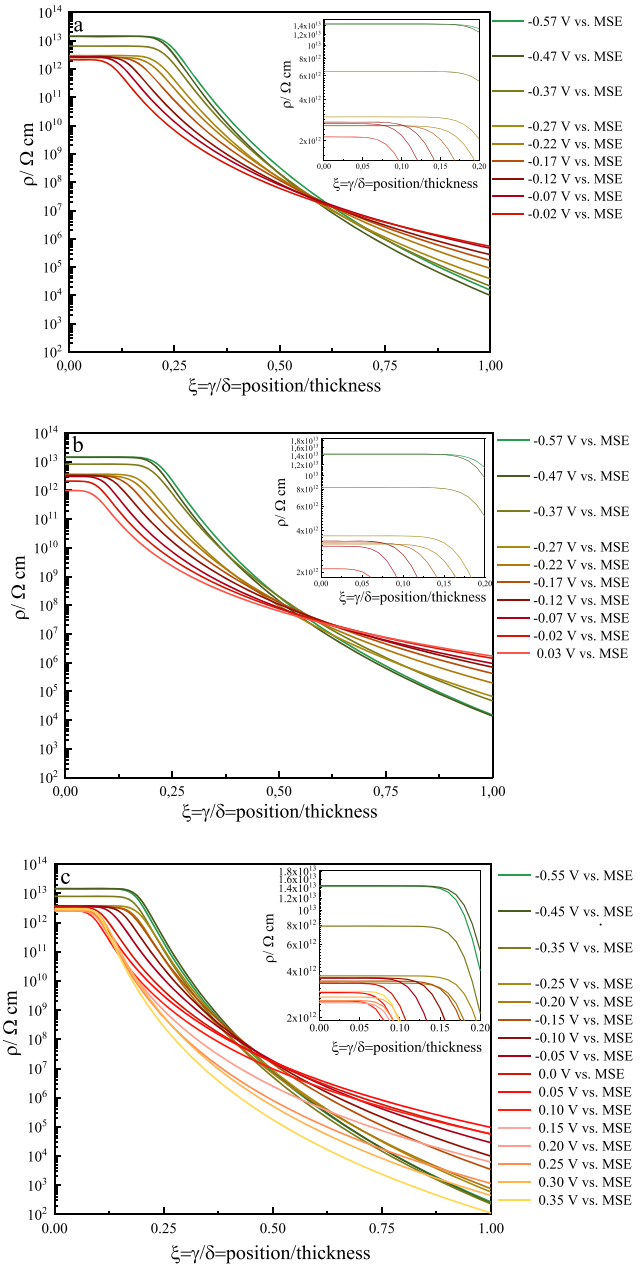

Figure 7. Distribution of resistivity within dimensionless thickness for (a) Ni–16Cr, (b) Ni–28Cr, and (c) Ni–14Cr–8Fe alloys in 0.05 M H_3BO_3 + 0.075 M $Na_2B_4O_7$ $10H_2O$ borate buffer solution (pH = 9.2).

of Ni–16Cr of 10^4 Ω cm. These findings suggest that Fe contributes to the outer layer of the passive film (likely in the hydroxide form) and acts as a defect, decreasing the local resistivity, but also that the presence of Fe plays a role in the passive film composition and structure by thinning the inner layer and inducing a more defective outer layer. However, the current density measured during polarization was similar, indicating that the inner layer acts as the barrier and that the electrochemical reaction at the metal/passive film interface is the limiting factor. Furthermore, ρ_δ for the Ni–14Cr–8Fe alloy reached a maximum of 10^5 Ω cm at the potential of 0.0 V vs MSE, which is close to that obtained for the Ni–16Cr alloy. With increasing applied potential, the consumption of defects occurs at the interface between the passive film and electrolyte, as for binary alloys. Because the passivation region of Ni–14Cr–8Fe has a longer passivation potential range than that for the Ni–30Cr–8Fe or Ni–xCr binary alloys, the evolution of the resistivity and resistivity profiles could be monitored over a wider potential range. When the applied potential increased up to 0.35 V vs MSE, ρ_0 remained constant (slight increase), whereas the length of the plateau decreased again. Concomitantly, a rapid decrease in ρ_δ was observed, indicating another possible change of the composition of the passive film in this potential range, corresponding to the XPS results presented in Fig. 4.

Role of the alloy composition on the passive and transpassive behaviors.—Figure 8 presents schematic representations of the evolution of the passive film grown on Ni–16Cr and Ni–14Cr–8Fe with the applied potential. The representation takes into account the XPS results and the previous discussion on the parameters obtained by analyzing the impedance diagram during polarization. A duplex representation of the passive film with inner oxide layer and outer hydroxide layer was selected, although it is important to mention that a transition model from a dense oxide to a completely hydrated outer layer would be more accurate.

For Ni–16Cr, the passive film formed in the passive potential domain was composed of Cr oxide and hydroxide, with the contribution of Ni oxide and Ni hydroxide (Fig. 4a). During polarization from OCP to transpassive potential, the thickness of the passive film remained almost stable and was not significantly affected. The thickness of the inner dense layer decreased, and the decay of resistivity through the passive film was smoother. These findings indicate that even if the inner dense layer is thinner, the oxide form in the passive film remains significant. The evolution of the resistivity profiles may be associated with the migration of cation vacancies and cations that progressively modify the inner and outer layers as the applied potential increases. The motion and release of Cr and Ni cations are both involved in governing the steady state. For Ni–14Cr–8Fe, the chemical composition of the passive layer is more complex. The contribution of Fe within the oxide–hydroxide network is non-negligible. During polarization within the passive domain, the impedance parameters obtained for Ni–14Cr–8Fe showed the same evolution as for Ni–16Cr, indicating similar evolution of the passive films. Moreover, if ρ_0 is similar for both materials, ρ_δ is lowest for Ni–14Cr–8Fe, suggesting that the addition of Fe promotes the generation and accumulation of point defects in the outer layer.

When the second oxidation occurs, the dissolution of Cr in the passive layer (according to Eq. 1) is clearly evidenced for Ni–16Cr by the current density peak in the polarization curves (Fig. 3a) and the presence of CrO_3 in the passive film at 0.1 V vs MSE. (Figure. 4b). Note that the contribution of the Ni hydroxide also increases between the passive film grown at −0.1 V and 0.1 V vs MSE. This evolution of chemistry within the passive film is correlated to a decrease of the passive film thickness (Fig. 6a). These results suggest that Ni plays a crucial role in the modification of the passive film during the second oxidation. Indeed, for pure Cr, the thickness and α dramatically decrease, proving that the second oxidation of Cr governs the interface reactivity and causes the thinning of the passive layer. For binary alloys, the presence of Ni compensates the second oxidation of Cr due to the stability of the nickel oxide in this potential range and This effect is greater when the Ni content is higher. Analysis of the XPS data reveals a slight modification of the oxide layer between 0.1 and 0.4 V vs MSE. Increases of the total oxide/hydroxide ratio and of the $Ni(OH)_2$ contribution are observed. The presence of Ni, which remains passivated in this potential range, delays the dissolution and oxidation of Cr or Cr_2O_3 from the alloy or passive film. This prevention effect is assisted by the presence of the underneath metal layer affected by the preferential oxidation of Cr during the passivation process and Ni enrichment. However, this second passivation was not sufficient to prevent degradation of the alloys: this layer was thin, the current density was rather high, and the metal grain boundaries were etched, suggesting that preferential diffusion and oxidation occurred there.

For Ni–14Cr–8Fe, the transpassive behavior was different. First, no anodic peak appeared on the polarization curve (Fig. 3b). Instead,

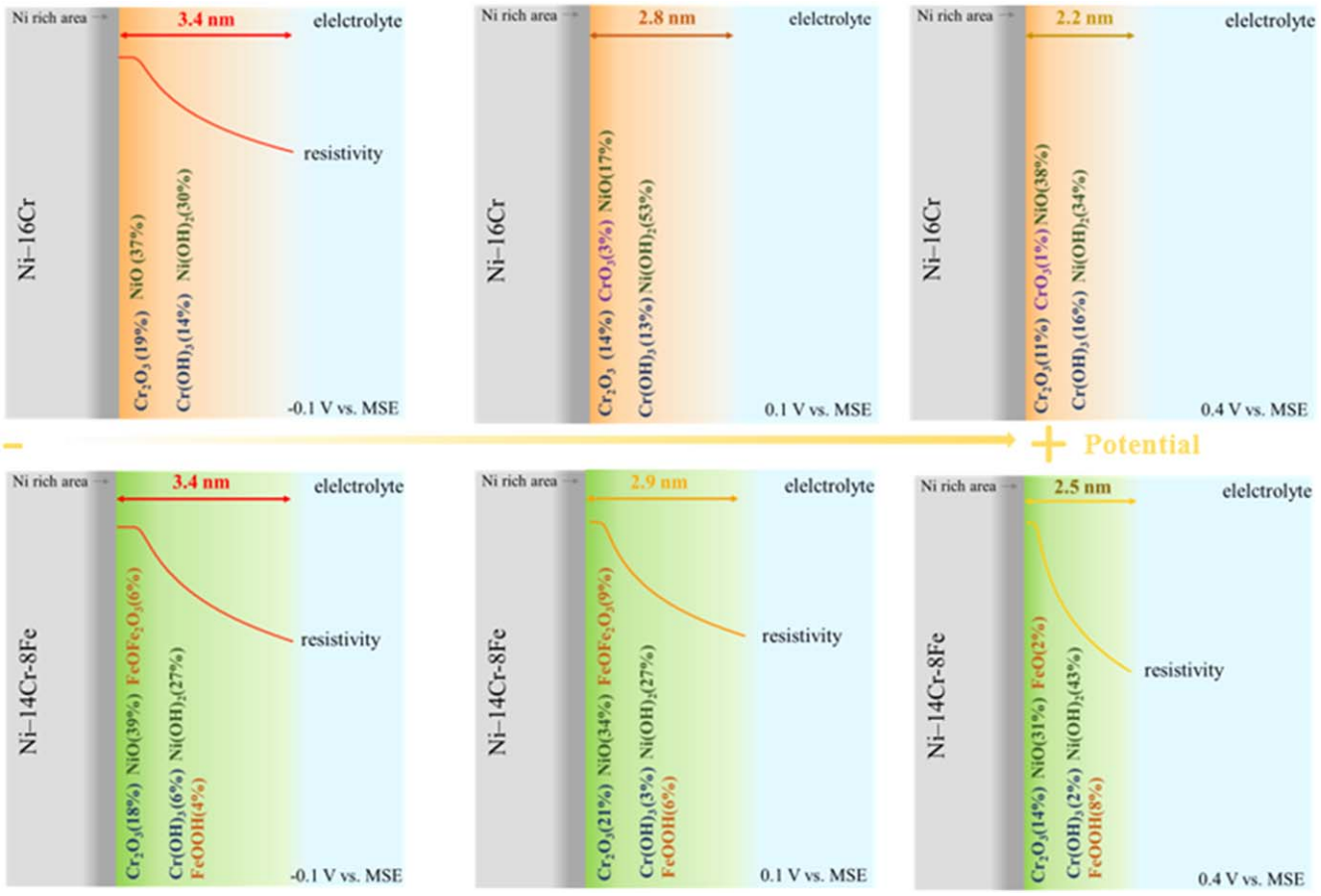

Figure 8. Schematic representation of the evolution of the passive film on Ni–16Cr and Ni–14Cr–8Fe alloy during polarization (from cathodic to anodic domains).

a singularity followed by a plateau was observed. Moreover, at 0.1 and 0.4 V vs MSE, CrO_3 was not detected by XPS in the passive film at these potentials. These findings indicate that the second oxidation of Cr is inhibited by the presence of Fe. Moreover, Palotta et al.[45] suggested that if CrO_3 is not detected by ex situ XPS analysis, a redox reaction may arise within the passive film between Fe (II) and Cr(VI) when the polarization is performed (reaction 10).

$$3Fe(II)_{film} + Cr(VI)_{film} \rightarrow Cr(III)_{film} + 3Fe(III)_{film} \quad [10]$$

The XPS analysis also revealed some differences between the passive films grown at 0.1 and 0.4 V vs MSE. The passive film grown at 0.4 V vs MSE was depleted in Cr (oxide and hydroxide forms) but enriched in Ni hydroxide. These results suggest that Fe within the passive film plays a complementary role, hindering the second oxidation peak and limiting the dissolution of Cr in basic solution. Then, the 8 wt.% Fe in the alloy may have a synergetic effect with Ni to limit the dissolution of the substrate and maintain a second passivation layer at potential higher than the Cr second oxidation potential. However, for Ni–30Cr–8Fe, the amount of Fe was not enough to prevent the anodic dissolution in the transpassive domain (Fig. 3b), resulting in a critical current density of 7 μA cm^{-2}, which is larger than the passive current density of 1 μA cm^{-2} on the Ni–14Cr–8Fe and Ni–22Cr–8Fe alloys.

Conclusions

The goal of this study was to highlight the role of the chemical composition of Ni-based alloys, essentially the Cr content and the addition of Fe, on their passive and transpassive behaviors in borate buffer solution. The electrochemical characterization was performed using successive impedance measurements over a wide potential range with the incorporation of recent advances in impedance diagram analysis. This innovative and in situ approach enabled monitoring of the evolution of the electrochemical parameters, physical parameters, and XPS data to better understand the modification within the passive film during polarization.

The polarization curves and parameters extracted from the impedance diagrams indicate that the Cr content in the alloy has no obvious effect on the passivation behavior of Ni–xCr in the passive potential domain. The normalized resistivity profiles showed the same duplex distribution and evolution despite the increased Cr content. However, the Cr content straightforwardly affects the electrochemical behavior of the alloys when transpassive dissolution occurs. A higher Cr content in the Ni–xCr alloys results in a higher current density peak in the transpassivation–second passivation processes. The Ni oxide or hydroxide could limit the oxidation of Cr to some extent.

Similarly, the addition of 8 wt.% Fe can diminish the current density peak related to the secondary passivation in the polarization curves. However, the dissolution peak cannot be completely reduced when the Cr content is high. The presence of Fe within the passive film tends to limit the dissolution of the alloys at high anodic potential by maintaining a passive layer at the surface of the alloy. XPS analysis also revealed an enrichment of Ni hydroxide in the passive film composition, indicating a synergetic effect of Fe and Ni to compensate the secondary oxidation of Cr.

With the help of successive impedance measurements and the power-law model, it was possible to obtain more information about passive films within the passivation domain, namely the evolution of the CPE parameters, thickness of the passive film, and resistivity profiles with applied potential. This measurement method might also

be employed for the study of commercial alloys or to design new alloys.

Acknowledgments

The authors acknowledge funding received from the region of Auvergne-Rhône-Alpes in France (grant: *SCUSI 2018/18 006577 01-22464*) and the China Scholarship Council (CSC) for the PhD grant for Zhiheng Zhang.

ORCID

Benoît Ter-Ovanessian https://orcid.org/0000-0002-1208-3689
Sabrina Marcelin https://orcid.org/0000-0002-6556-6879
Bernard Normand https://orcid.org/0000-0001-6255-8817

References

1. P. Marcus, *Corros. Sci.*, **36**, 2155 (1994).
2. T. Jabs, P. Borthen, and H. H. Strehblow, *J. Electrochem. Soc.*, **144**, 1231 (1997).
3. E. McCafferty, *Corros. Sci.*, **44**, 1393 (2002).
4. M. Bojinov, G. Fabricius, P. Kinnunen, T. Laitinen, and K. Ma, *Electrochim. Acta*, **45**, 2791 (2000).
5. H. H. Uhlig, *Zeitschrift für Elektrochemie, Berichte der Bunsengesellschaft für physikalische Chemie*, **62**, 700 (1958).
6. J. R. Myers, F. H. Beck, and M. G. Fontana, *Corrosion*, **21**, 277 (1965).
7. B. Ter-Ovanessian and B. Normand, *J. Solid State Electrochem.*, **20**, 9 (2016).
8. B. Ter-Ovanessian, N. Mary, and B. Normand, *J. Electrochem. Soc.*, **163**, 410 (2016).
9. G. Song, *Corros. Sci.*, **47**, 1953 (2005).
10. I. Betova, M. Bojinov, T. Laitinen, and M. Kari, *Corros. Sci.*, **44**, 2675 (2002).
11. Z. Zhang, B. Ter-Ovanessian, S. Marcelin, and B. Normand, *Electrochim. Acta*, **353**, 136531 (2020).
12. A. K. Mishra, S. Ramamurthy, M. Biesinger, and D. W. Shoesmith, *Electrochim. Acta*, **100**, 118 (2013).
13. A. K. Mishra and D. W. Shoesmith, *Electrochim. Acta*, **102**, 328 (2013).
14. F. Hamdani, *Improvement of the corrosion and oxidation resistance of Ni-based alloys by optimizing the chromium content*, INSA Lyon (2016), http://theses.insa-lyon.fr/publication/2015ISAL0012/these.pdf.
15. N. Jallerat, S. Mischler, and D. Landolt, *Modifications of Passive Films*, ed. P. Marcus, B. Baroux, and M. Keddam (The Institute of Materials, London, UK) EFC Publication 12,26 (1993) .
16. S. Boudin, J.-L. Vignes, G. Lorang, M. D. C. Belo, G. Blondiaux, S. M. Mikhailov, J. P. Jacobs, and H. H. Brongersma, *Suface and interface analysis*, **22**, 462 (1994).
17. M. Da Cunha, N. E. Hakiki, and M. G. S. Ferreira, *Electrochim. Acta*, **44**, 2473 (1999).
18. B. Normand, N. Bererd, P. Martinet, S. Marcelin, M. Moine, J. Feirrera, D. Baux, T. Sauvage, and N. Moncoffre, *Corros. Sci.*, **176**, 108945 (2020).
19. K. T. Chiang, D. S. Dunn, and G. A. Cragnolino, *Corrosion*, **63**, 940 (2007).
20. W. Ye, Y. Li, and F. Wang, *Electrochim. Acta*, **54**, 1339 (2009).
21. D. Marijan, M. Gojic, and P. Industry, *J. Appl. Electrochem.*, **32**, 1341 (2002).
22. D. Rai, B. M. Sass, and D. A. Moore, *Inorg. Chem.*, **26**, 345 (1987).
23. V. Jovancicevic, P. Zelenay, and B. R. Scharifker, *Electrochim. Acta*, **32**, 1553 (1987).
24. S. E. L. Euch, D. Bricault, H. Cachet, E. M. M. Sutter, M. T. T. Tran, V. Vivier, N. Engler, A. Marion, M. Skocic, and B. Huerta-Ortega, *Electrochim. Acta*, **317**, 509 (2019).
25. C. D. Wagner, R. H. Raymond, and L. H. Gale, *Surf. Interface Anal.*, **3**, 211 (1981).
26. S. Marcelin, B. Ter-Ovanessian, and B. Normand, *Electrochem. Commun.*, **66**, 62 (2016).
27. S. Marcelin, Z. Zhang, B. Ter-Ovanessian, and B. Normand, *J. Electrochem. Soc.*, **168**, 021503 (2021).
28. M. E. Orazem, N. Pébère, and B. Tribollet, *J. Electrochem. Soc.*, **153**, B129 (2006).
29. M. E. Orazem and B. Tribollet, *Electrochemical Impedance Spectroscopy* (Wiley, London, UK) 2nd ed. (2017).
30. S. Chakri, I. Frateur, M. E. Orazem, E. M. M. Sutter, T. T. M. Tran, B. Tribollet, and V. Vivier, *Electrochim. Acta*, **246**, 924 (2017).
31. M. Benoit, C. Bataillon, B. Gwinner, F. Miserque, M. E. Orazem, C. M. Sánchez-sánchez, B. Tribollet, and V. Vivier, *Electrochim. Acta*, **201**, 340 (2016).
32. B. Lovreček and J. Sefaja, *Electrochim. Acta*, **17**, 1151 (1972).
33. B. Hirschorn, M. E. Orazem, B. Tribollet, V. Vivier, I. Frateur, and M. Musiani, *J. Electrochem. Soc.*, **157**, C452 (2010).
34. B. Hirschorn, M. E. Orazem, B. Tribollet, V. Vivier, I. Frateur, and M. Musiani, *J. Electrochem. Soc.*, **157**, C458 (2010).
35. K. Lutton Cwalina, C. R. Demarest, A. Y. Gerard, and J. R. Scully, *Curr. Opin. Solid State Mater. Sci.*, **23**, 129 (2019).
36. S. Ahn, H. Kwon, and D. D. Macdonald, *J. Electrochem. Soc.*, **152**, B482 (2005).
37. W.-S. Kim, *Electrochemical Characterization of Passive Films Formed on Ni Based Alloys*, Osaka University (2015).
38. C. Man, C. Dong, Z. Cui, K. Xiao, Q. Yu, and X. Li, *Appl. Surf. Sci.*, **427**, 763 (2018).
39. Z. Feng, X. Cheng, C. Dong, L. Xu, and X. Li, *Corros. Sci.*, **52**, 3646 (2010).
40. L. A. Toledo-matos and M. A. Pech-canul, *J. Solid State Electrochem.*, **15**, 1927 (2011).
41. J. S. Kim, E. A. Cho, and H. S. Kwon, *Electrochim. Acta*, **47**, 415 (2001).
42. M. Bojinov, G. Fabricius, P. Kinnunen, T. Laitinen, K. Mäkelä, T. Saario, G. Sundholm, and K. Yliniemi, *Electrochim. Acta*, **47**, 1697 (2002).
43. H. Tsuchiya, S. Fujimoto, O. Chihara, and T. Shibata, *Electrochim. Acta*, **47**, 4357 (2002).
44. B. Krishnamurthy, R. E. White, and H. J. Ploehn, *Electrochim. Acta*, **47**, 3375 (2002).
45. C. D. Pallotta, S. Hild, and E. Garcia, *J. Electrochem. Soc.*, **135**, 314 (1988).